Rational Design of Rhodium-Iridium Alloy Nanoparticles as Highly Active Catalysts for Acidic Oxygen Evolution

Hongyu Guo, [†,§] *Zhiwei Fang,* [‡,§] *Hao Li,* [†] *Desiree Fernandez,* [†] *Graeme Henkelman,*,*[†] *Simon M. Humphrey,*,* [†] *and Guihua Yu*,*[‡]

[†] Department of Chemistry, The University of Texas at Austin, Austin, Texas 78712, United States

[‡] Materials Science and Engineering Program and Department of Mechanical Engineering, The University of Texas at Austin, Austin, Texas 78712, United States

ABSTRACT: The oxygen evolution reaction (OER) is pivotal for renewable energy conversion and storage devices, such as water electrolyzers and rechargeable metal-air batteries. However, rational design of electrocatalysts with suitably high efficiencies and stabilities in strongly acidic electrolytes remains a significant challenge. Here, we show the demonstration of sub-10 nm, composition-tunable Rh-Ir alloy nanoparticles (NPs) prepared using a scalable microwave-assisted method as superior acidic OER catalysts. The OER activities showed a volcano-shaped dependence on Ir composition, with Ir-rich NPs (Ir ≥51%) achieving better OER performance than pure Ir NPs, as reflected by lower overpotentials and higher mass activities. Most significantly, $Rh_{22}Ir_{78}$ NPs achieved a maximum mass activity of 1.17 A mg^{-1}_{Ir} at a 300 mV overpotential in 0.5 M H_2SO_4, which corresponds to a 3-fold enhancement relative to pure Ir NPs, making it one of the most active reported OER catalysts under acidic conditions. Density functional theory (DFT) calculations reveal that owing to the synergy of ensemble and electronic effects by alloying a small amount of Rh with Ir, the binding energy difference of the O and OOH intermediates are reduced, leading to faster kinetics and enhanced OER activity. Furthermore, Rh-Ir alloy NPs demonstrated excellent durability in strongly acidic electrolyte. This work not only provides fundamental understandings relating to composition-electrochemical performance relationships but also represents the rational design of highly efficient OER electrocatalysts for applications in acidic media.

KEYWORDS: rhodium-iridium alloy, oxygen evolution reaction, acidic electrolyte, microwave synthesis, ensemble effect

Developing active and durable catalysts is of foremost importance for the large-scale deployment of efficient and ecologically friendly energy storage and conversion devices, such as rechargeable metal-air batteries and water electrolyzers.[1–3] In these systems, the anodic half-reaction, known as the oxygen evolution reaction (OER), plays a substantial role. This reaction mechanism involves multiple electron transfer processes, which suffer from sluggish kinetics and the requirement for large applied overpotentials compared to the cathodic reaction.[4,5] Although significant advances have been achieved in the design of OER catalysts that can operate in neutral and basic OER electrolytes,[6–14] the identification of efficient and stable OER electrocatalysts that can tolerate acidic electrolytes is still a largely unsolved challenge. Nonetheless, this challenge is attractive because acidic electrolytes exhibit distinctive advantages over alkaline electrolytes for OER, providing access to higher ionic conductivities and eliminating the formation of undesirable carbonate contaminants.[15–17] Until now, Ir-based materials have been regarded as state-of-the-art OER catalysts in acidic media,[1,18–21] yet the low abundance of Ir is a major restriction to their widespread application. For this reason, careful selection of synthetic approaches is required to identify Ir-based catalysts with enhanced OER performance.

Extensive efforts combining theoretical and experimental approaches suggest the binding energy of oxygen-containing intermediates play a crucial role in determining catalytic OER activity.[22–25] Various strategies of composition engineering such as doping heteroatoms into IrO_2 or designing Ir-based alloys[26–29] have been shown to be effective for tuning the binding strength of O intermediates through synergistic effects (*e.g.* ensemble, electronic and strain effects), thus enhancing the intrinsic activity of each active site.[30–36] For example, a recent study suggests that the crystal lattice strain induced by the introduction of smaller lanthanide atoms into iridium-based double perovskite materials can lower the O adsorption energy, which results in a threefold

increase in OER performance.[26] Guo and coworkers suggested that alloying Ir with Ni and Co on the nanoscale can shift the d-band away from Fermi level, which weakens binding of surface hydroxyl intermediates, leading to a ten-fold increase in the measured OER turnover frequency (TOF) compared to commercial Ir/C catalysts.[28] Qiao and coworkers demonstrate that the leaching of Co from Co-doped RuIr alloy electrocatalyst results in the increase of O^{I-} species and the promotion of OER performance.[29] Meanwhile, downsizing the catalyst NP dimensions to a few nanometers is also commonly employed to increase the density of specific active sites, while simultaneously improving Ir atom utilization; together, this can lead to improved OER performances in terms of higher effective mass activities. Ir-containing alloy nanoparticles are more attainable than Ir-based oxide nanoparticles. Therefore, the rational design of unexplored Ir alloy nanoparticle systems to enable comprehensive studies of the relationships between composition, binding energies and electrocatalytic performances remains highly desirable.

Although Ir-Fe, Ir-Co, Ir-Ni and Ir-W alloy NPs have been successfully synthesized and demonstrated as highly active OER catalysts,[37-39] examples of Ir-based alloy NPs remain quite limited. Furthermore, the majority of previous studies have focused on specific alloy compositions but have not addressed whether fine-tuning the composition can be exploited to further optimize the binding energy of OER intermediates. Commonly, these issues stem from synthetic difficulties pertaining to the synthesis of Ir-based alloy NPs across broad composition ranges, or with desired compositions. In fact, Ir is broadly immiscible with most other metals in the periodic table.[40,41] Therefore, the determination of 'bottom-up' wet synthetic methods is very timely in order to provide systematic access to a greater library of kinetically stable NP catalysts. Our recent study demonstrated that Ag-Ir alloy NPs could be synthesized under microwave irradiation, while conventional oil bath heating resulted in separate reduction of Ag and Ir precursors.[41] Hence, it is

appealing to develop unconventional and systematic approaches for the generation of Ir-based alloy NPs with tunable compositions.

Here, we report the microwave-assisted synthesis of $Rh_xIr_{(100-x)}$ alloy NPs covering a wide composition range (x=22–73). Although pure Rh usually shows relatively lower OER activities as compared to pure Ir,[42,43] electronic and strain effects *via* alloying are expected to help further tune the adsorbate binding at those pure-Ir sites in an RhIr alloy surface.[32] These synergetic alloying effects can optimize the active Ir-sites for OER, leading to expected higher overall OER activity. These NPs display excellent OER activities and durability in an acidic electrolyte (Figure 1A). In a series of $Rh_xIr_{(100-x)}$ NPs, $Rh_{22}Ir_{78}$ NPs displayed the highest mass activity of 1.17 A mg^{-1}_{Ir} with an associated TOF of 5.10 s^{-1}; these values are among the best reported OER catalysts in acidic media. Negligible polarization curve shifts were also observed after 2000 OER cycles, indicating very high stability of the Rh-Ir alloys. DFT calculations also suggest that alloying a small amount of Rh (22 at%) with Ir results in a minimal binding energy difference between O and OOH intermediates, thus accelerating the OER rate-determining step and enhancing OER activity relative to pure Ir NPs. This work not only represents the exploration of a rational design of alloy NP system but also highlights the significance of fine-tuning of catalyst composition in order to boost electrocatalytic OER performance.

RESULTS AND DISCUSSION

In this work, $Rh_xIr_{(100-x)}$ NPs were prepared using a modified polyol method. Briefly, a mixed solution of $IrCl_3$ and $RhCl_3$ was injected into a pre-heated ethylene glycol (EG) solution containing polyvinylpyrrolidone (PVP) at 150 °C inside a CEM-MARS-5 microwave reactor under continuous microwave irradiation. The addition rate of the metal precursor solution was controlled at 6.0 mmol h^{-1} using a syringe pump. The initially red-colored solution of metal precursors

quickly turned black, indicating the rapid formation of metallic NPs. The resulting mixture was irradiated for 30 min before being quenched in an ice-water bath. The NPs obtained were collected by centrifugation, followed by washing with ethanol/hexanes to remove excess PVP and spectator ions (see Supporting Information for more details). The ratio of $RhCl_3$ to $IrCl_3$ was adjusted to be 1:3, 1:1 and 3:1 to achieve NPs with three different compositions.

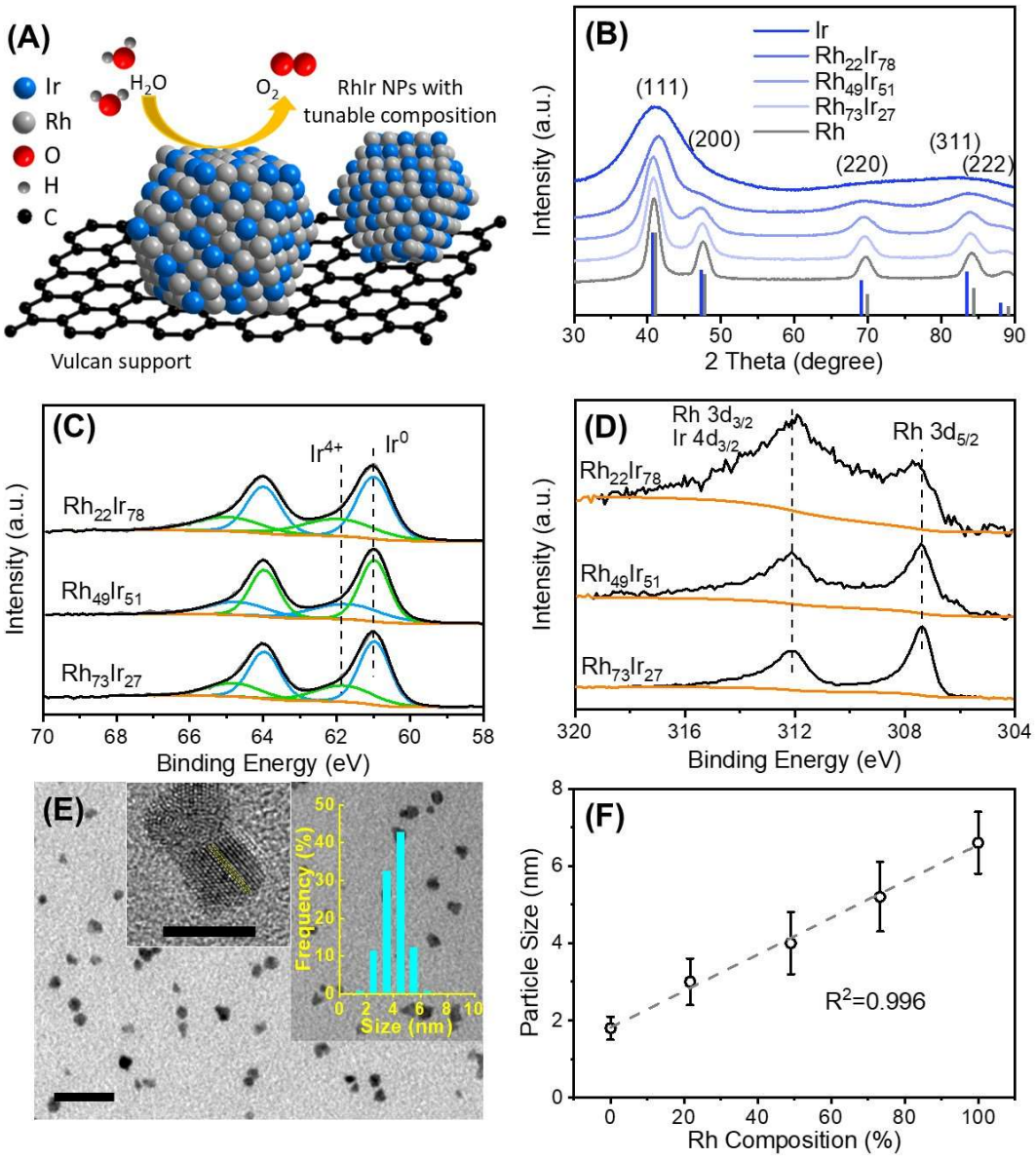

Figure 1. (A) Schematic illustration of $Rh_xIr_{(100-x)}$ NPs supported on Vulcan XC-72R carbon for OER in acidic media. (B) PXRD patterns for Ir NPs, Rh NPs and $Rh_xIr_{(100-x)}$ NPs with different compositions; standard PXRD reflection positions for Ir (dark blue line, JCPDS card#006-0598) and Rh (grey line, JCPDS card#005-0685) are also shown for reference. (C) XPS spectra of the Ir 4f region for $Rh_xIr_{(100-x)}$ NPs. (D) XPS spectra of the Rh 3d region for $Rh_xIr_{(100-x)}$ NPs. (E) TEM image of $Rh_{49}Ir_{51}$ NPs; scale bar equals to 20 nm. Insets: size distribution histogram and HRTEM image showing the lattice fringes of (111) planes; inset scale bar equals to 5 nm. (F) Average particle size as a function of Rh composition.

A combination of characterization techniques was employed to understand the composition, structure and morphology of the as-synthesized NPs. According to the results of inductively coupled plasma optical emission spectroscopy (ICP-OES), Rh-Ir NPs with broad composition range could be prepared by tuning the ratio of metal precursors (Table S1), to provide products with bulk compositions that closely mirrored the nominal compositions. Henceforth, the compositions of all Rh-Ir NPs in this work are denoted based on the compositions determined by ICP-OES. Powder X-ray diffraction (PXRD) indicated that Rh-Ir nanoparticles adopted a face-centered cubic (FCC) structure, consistent with both pure Ir and Rh (Figure 1B). The d-spacing of (220) reflection showed a linear composition dependence, indicating the homogenous solid-solution structures of the alloy NPs (Figure S1). However, we found that NPs with Ir-rich compositions exhibited broader reflections, suggesting a decrease of particle size with increasing Ir content. X-ray photoelectron spectroscopy (XPS) was used to confirm the chemical states of the alloy NPs. The majority of Ir in the Rh-Ir NPs was in its Ir(0) metallic state, with a binding energy of Ir $4f_{7/2}$ at 60.9 eV.[44] Meanwhile, a minor peak at a binding energy of 61.5 eV was also observed, representing IrO_2 species generated from inevitable surface oxidation during the synthesis and

purification processes (Figure 1C). Unfortunately, due to the overlap of Rh 3d and Ir 4d signals, it was difficult to analyze the surface oxidation of Rh using XPS, especially for NPs with Ir-rich compositions (Figure 1D).

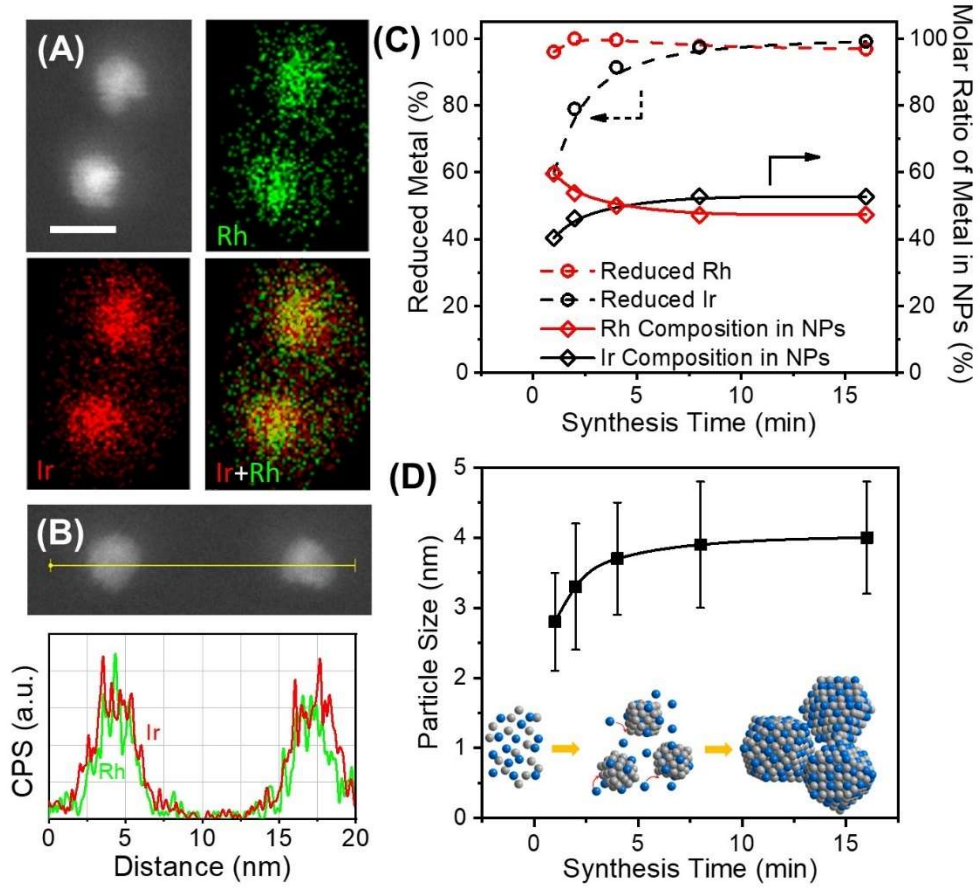

Figure 2. (A) HAADF-STEM image for two $Rh_{49}Ir_{51}$ NPs and the corresponding EDS elemental mapping showing Rh, Ir and overlay signal; scale bar equals to 5 nm. (B) EDS line scan profile for two $Rh_{49}Ir_{51}$ NPs with corresponding elemental counts. (C) The reduced metal precursor percentage and the composition of Rh-Ir NP intermediates as a function of synthesis time. (D) Particle size of Rh-Ir NP intermediates as a function of synthesis time. Inset: schematic illustration of NP formation process; blue and grey spheres represent Ir and Rh atoms, respectively.

Transmission electron microscopy (TEM) imaging revealed that $Rh_xIr_{(100-x)}$ NPs of all compositions were cuboctahedral-shaped (Figures 1E and S2). Size analysis based on measurements of at least 300 NPs clearly indicates that the particle size of the Rh-Ir alloy NPs has a direct composition dependence, with the average size increasing linearly with higher Rh content (Figure 1F). The lattice spacing of $Rh_{49}Ir_{51}$ NPs was measured to be 0.220 nm from high-resolution TEM images, which corresponds well to the expected spacing for the (111) planes in FCC packing (Figure 1E, inset). Rh-Ir alloy NPs with different compositions did not show a marked change in the measured d-spacing, owing to the similar lattice constants of Rh and Ir (Figure S2). Energy dispersive spectroscopy (EDS) in 2-D elemental mapping mode was used to further study the nanoalloy structure of individual particles. Examination of $Rh_{49}Ir_{51}$ NPs indicated that Rh and Ir were indeed homogeneously distributed within the NPs; the estimated composition from the EDS data gave Rh:Ir = 44:56, in good agreement with the results of ICP-OES (Figures 2A and S3). EDS line scanning also showed no evidence of segregation of Rh or Ir near the NP surfaces, providing further evidence of uniform solid-solution Rh-Ir structures throughout the NPs (Figure 2B). Similarly, homogeneous alloying was also observed for $Rh_xIr_{(100-x)}$ NPs with other compositions (Figure S4).

To better understand the formation mechanism of $Rh_xIr_{(100-x)}$ NPs, the kinetics of alloy formation was studied in more detail using $Rh_{50}Ir_{50}$ as a nominal target NP composition. About 0.5 ml aliquots were removed from the reaction at regular intervals during synthesis and aliquots were immediately transferred to an ice-water bath to prevent further growth of the NPs. The solid NPs were separated from any possible unreduced precursors by centrifugation. ICP-OES analysis indicated that the Rh(III) precursor was reduced almost immediately after being added to hot EG (60 s), with all the Rh ions converting to metallic state after the precursor addition step. In contrast,

only about 60% of the Ir(III) ions had apparently been reduced at this time, resulting in the early NP seeds having a Rh-rich composition of approximately $Rh_{60}Ir_{40}$ (Figure 2C); the corresponding average particle size was confirmed to be 2.8 ±0.7 nm by TEM (Figures 2D and S5). After further heating of 60 s and 180 s, 79% and 91% of the iridium species were incorporated into the NPs, respectively, with a corresponding increase of the average NP size to 3.3 ±0.9 and 3.7 ±0.8 nm, respectively. The average compositions of these NPs were determined to be $Rh_{54}Ir_{46}$ and $Rh_{50}Ir_{50}$ in bulk respectively, by ICP-OES. These observations suggest that Rh precursors are reduced faster than Ir precursors, leading to the generation of Rh-rich nucleates at the beginning of the synthesis, while a proportion of Ir(III) ions become reduced at the growing NP surfaces (*i.e.*, by autocatalytic reduction) to form the final alloy structures over a period of several minutes.[45] ICP-OES results indicate that >97% of the Ir precursors were reduced at 8 min of synthesis time, while no obvious compositional or size differences were noted at longer reaction times (*i.e.* 16 and 30 min), suggesting that the NP formation reached completion under microwave irradiation after only 8 min.

Since Ir-based materials are widely considered as benchmark catalysts for OER in acidic electrolytes, OER was next utilized to assess the electrocatalytic activities of supported $Rh_xIr_{(100-x)}$ NPs as a function of the Rh:Ir composition. Before the electrochemical measurements, $Rh_xIr_{(100-x)}$ NPs were first deposited on Vulcan XC-72R carbon black through a simple wet impregnation method (see Supporting Information for more details). Monometallic Rh and Ir NPs were also prepared using the same microwave-based method and using the same capping agent. The monometallic NPs were deposited on Vulcan carbon in the same fashion to provide control electrocatalysts for comparison to the alloys. Next, the catalyst materials were treated with a solution of *tert*-butyl amine and $NaBH_4$ to remove the PVP capping agent from the NP surfaces.[46]

The actual %wt total metal loading (Rh+Ir) was determined for each catalyst by ICP-OES analysis; all catalysts had loadings within the desired range of 4-5 wt% (Table S1). TEM images of the pristine supported electrocatalysts confirmed that NPs were evenly distributed on the surface of Vulcan support without obvious agglomeration (Figure S6).

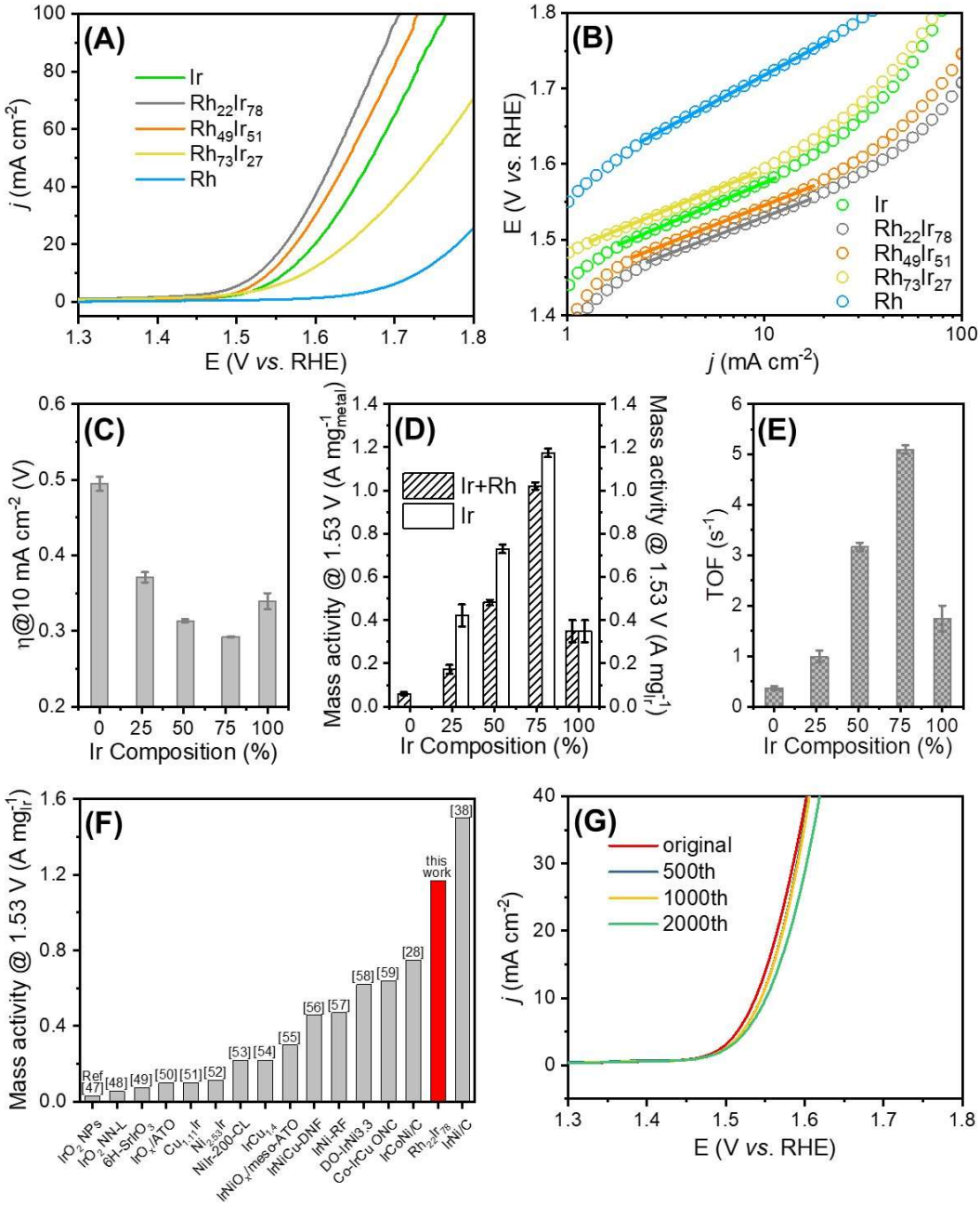

Figure 3. (A) IR-corrected OER polarization curves for Ir/VXC, Rh/VXC and $Rh_xIr_{(100-x)}$/VXC with different compositions measured in 0.5 M H_2SO_4 aqueous solution. (B) Tafel plots of the electrocatalysts. (C) Bar graph showing the overpotential Ir/VXC, Rh/VXC and $Rh_xIr_{(100-x)}$/VXC needed to reach a current density of 10 mA cm^{-2}. (D) The mass activity at 1.53 V *vs*. RHE normalized by both Ir and overall metal content, as a function of Ir composition. (E) Turnover frequencies normalized by the ECSA for different catalysts at 1.53 V *vs*. RHE. (F) Summary of representative works of Ir-based OER catalysts with their respective mass activity at 1.53 V *vs*. RHE in acidic media. NN-L: long nanoneedle; CL: after chemical leaching; DNF: double-layered nanoframe; RF: rhombic dodecahedral nanoframe; DO: coupled dealloying/oxidation; ONC: octahedral hollow nanocage. (G) IR-corrected OER polarization curves for $Rh_{22}Ir_{78}$/VXC after 500, 1000 and 2000 OER cycles.

All electrochemical measurements were conducted after catalyst activation in an aqueous solution of 0.5 M H_2SO_4, using a scan rate of 10 mV s^{-1}. The IR-corrected polarization curves revealed that the OER catalytic performances of catalysts with different compositions were in the following order: $Rh_{22}Ir_{78}$/VXC > $Rh_{49}Ir_{51}$/VXC > Ir/VXC > $Rh_{73}Ir_{27}$/VXC >> Rh/VXC (Figure 3A), indicating a significant improvement of OER performance for the more Ir-rich compositions *versus* pure Ir NPs; in line with this finding, the Rh-rich Rh-Ir electrocatalysts also out-performed pure Rh NPs. Notably, the most active $Rh_{22}Ir_{78}$/VXC material showed the smallest Tafel slope among all the compositions, indicating a larger charge-transfer coefficient and a faster kinetics (Figure 3B and Table S2). Furthermore, it only required an overpotential of only 292 mV to achieve a current density of 10 mA cm^{-2}, which is 48 mV lower than the 340 mV overpotential of Ir/VXC (Figure 3C and Table S2). Commercial Ir/C (Premetek, 5 wt% Ir nanoparticles supported on Vulcan XC-72) and IrO_2/VXC with similar loading of Ir were also examined for comparison,

with both shown to display lower OER performance (Figures S7-8). The corresponding mass activity of $Rh_{22}Ir_{78}$/VXC at an overpotential of 300 mV was measured to be 1.02 A mg^{-1}_{metal} and 1.17 A mg^{-1}_{Ir}, which is three times more active than Ir/VXC (0.349 A mg^{-1}_{metal}) (Figure 3D). These values confirm that $Rh_{22}Ir_{78}$/VXC is one of the most active Ir-based OER catalysts reported to-date (Figure 3F, Table S3).[28,38,47-59] Following $Rh_{22}Ir_{78}$/VXC, $Ir_{49}Ir_{51}$/VXC also achieved a higher OER activity surpassing Ir/VXC, as reflected by its lower overpotential, higher current density and mass activity. Although $Rh_{73}Ir_{27}$/VXC showed a larger overpotential, it still also exhibited higher mass activity in terms of Ir content (0.422±0.050 A mg^{-1}_{Ir}) than Ir/VXC, demonstrating an improved activity of Ir sites by Rh. In order to eliminate the contribution of diverse particle size to the OER performance, the electrochemical surface areas (ECSA) of Ir/VXC, Rh/VXC and $Rh_xIr_{(100-x)}$/VXC were measured by integrating the H underpotential deposition area from cyclic voltammetry (CV) (Figure S9). The intrinsic activity of $Rh_xIr_{(100-x)}$ NPs was then evaluated by calculating the ECSA-normalized TOFs. The resulting ECSA-normalized TOFs displayed the same trend as for the mass activities (Figure 3E, Table S4). These results confirm that there is a direct influence of surface Ir concentration upon OER activity.

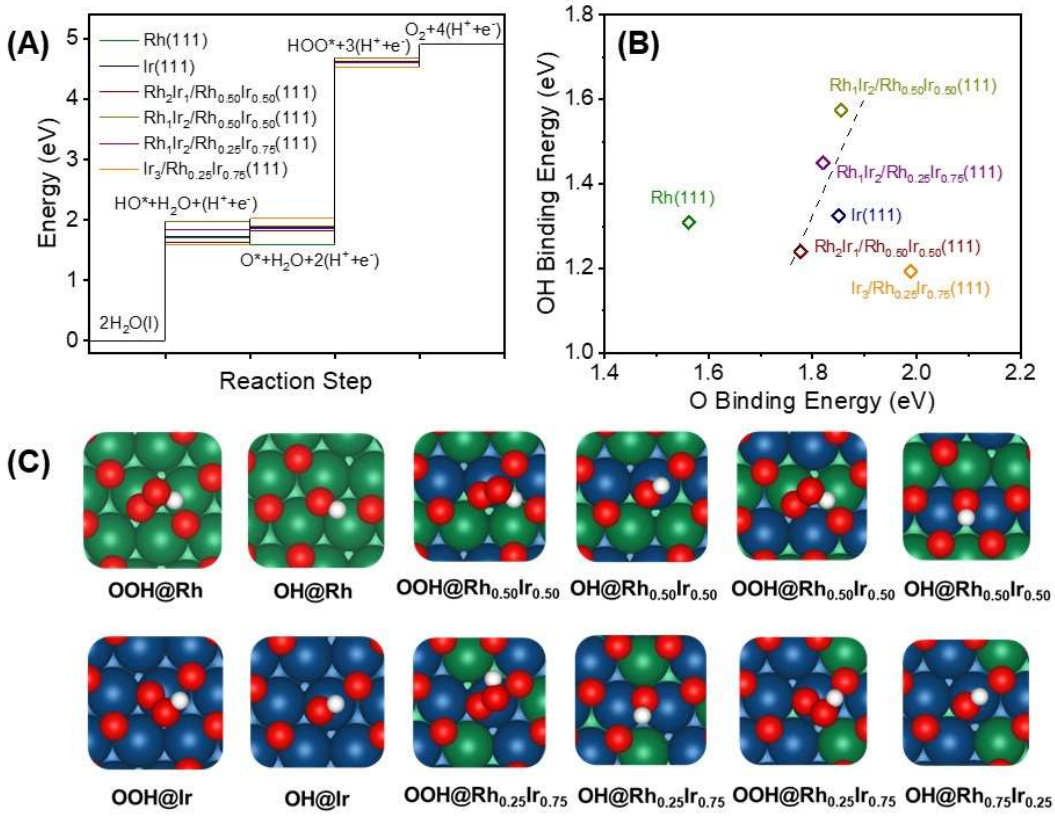

Figure 4. (A) Calculated free energy pathways for oxygen evolution reaction on Rh (111), Ir (111), and $Rh_xIr_{(1-x)}$ (111) (x = 0.25 and 0.50). (B) O *versus* OH binding energies at the studied surfaces. (C) The optimized geometries of reaction adsorbates on the surfaces; green = Rh, blue = Ir, red = O, white = H.

To understand the trend of OER activity shown in Figure 3, DFT calculations were conducted to acquire the reaction free energies of OER on Rh (111), $Rh_xIr_{(1-x)}$ (111) (x=0.25 and 0.50), and Ir (111) surfaces (Figure 4A) using the computational hydrogen electrode (CHE) method (Equations S3-S6),[60] since the (111) surface is more stable compared with the higher energy (100) surface in cuboctahedral NPs under OER conditions. The edge and corner sites of NPs are expected to be inactive in this particular catalytic reaction because the OOH intermediate binds too strongly at these under-coordinated sites, resulting in passivation of the sites.[61] Since the three-fold hollow

site is the smallest ensemble providing the complete adsorption environment of an adsorbate, which in turn determines the catalytic activity at the close-packed alloy surfaces,[33] our discussion focuses on these three-fold ensembles. In the calculations, the surface model was pre-covered with oxygen atoms to match the experimental XPS results, showing that the NPs are mostly metallic before and after OER (Figure 1C and Figure S10), so that the surface of the NPs was allowed to become partially oxidized. Therefore, we did not consider other models such as complete oxides and ligand-anchored metallic surfaces.[60,62] Additional discussion of the modeling can be found in the Supporting Information. Using Equation S7, it can be seen that the formation of OOH* is the rate-determining step at all these surface sites. The theoretical overpotentials of pure Ir (111) and Rh (111) were calculated to be 1.50 and 1.80 V, suggesting that Ir is intrinsically more active than Rh. Therefore, we only evaluated alloys with equal-Ir-Rh and Ir-rich compositions. On a Rh-Ir alloy (111) surface with bulk compositions of $Rh_{0.50}Ir_{0.50}$ and $Rh_{0.25}Ir_{0.75}$, both the Ir_1Rh_2 and Ir_2Rh_1 triatomic ensembles have theoretically-predicted overpotentials that lie between pure Ir (111) and Rh (111), while Ir_3 ensembles on a $Rh_{0.25}Ir_{0.75}$ (111) surface possess the lowest overpotential (1.28 V) of all sites considered in this study (Table S5). The low overpotential at the Ir_3 site on $Rh_{0.25}Ir_{0.75}$ (111) originates from the deviation from the scaling relationship between O and OH binding energies, yielding a weaker O binding than the general trend (Figure 4B). This further leads to smaller binding energy differences between O and OOH intermediates, leading to an acceleration of this crucial OER rate-determining step. Since Ir_3 ensembles dominate the surfaces of NPs with Ir-rich compositions, this explains the observed experimental results, in that alloying a smaller amount of Rh into Ir lead to the greatest enhancement in OER activity under acidic conditions (Figure 3). It should be noted that the values of the theoretical and experimental overpotentials should not be compared directly, as the experimental overpotentials are further affected by factors

such as the adsorbate coverage[32] and different reactive surface area which originated from different sizes of the NPs.[63] However, the DFT calculations are in good qualitative agreement with experimental results.

The durability of the most active $Rh_{22}Ir_{78}$/VXC catalyst was then assessed by cycling the potential between 1.1─1.5 V (*vs*. Ag/AgCl) at a scan rate of 10 mV s^{-1} over 2000 consecutive cycles and a chronopotentiometry test at 1.53 V (*vs*. RHE). The excellent stability of the catalyst was verified by only a minor increase in its overpotential (13 mV) after 2000 cycles (Figure 3G), and a maintenance of 85% of initial current density after 8 h measurement. In comparison, the current density of commercial Ir/C decreased by 65% after 2 h in chronopotentiometry test (Figure S11). After the durability test, the same catalyst material was thoroughly characterized to understand any structural changes caused by exposure to prolonged acidic OER conditions. XPS measurements were performed to investigate the surface oxidation state for $Rh_{22}Ir_{78}$/VXC before and after the durability test. The deconvoluted Ir 4f region of the XPS spectrum of the post-OER catalyst indicated oxidation of the surface Ir(0) atoms to Ir(IV) and a significant amount of higher valent Ir ($Ir^{>4+}$) during the strongly anodic conditions under prolonged durability testing, which is consistent with previous reports (Figure S12).[56,59] Although no Ir(0) signal was observed in the XPS spectrum, lattice fringes with distances corresponding to metallic Rh-Ir (111) planes were still clearly observed in the HRTEM images (Figure S13). A closer investigation of the XPS spectrum revealed an abundance of Nafion on the surface of the catalyst after durability test, as evidenced by the presence of a strong F 1s signal (Figure S14). Since XPS is a surface technique with an intrinsic detection depth of only a few nanometers from the surface, the buildup of a Nafion layer around the NPs is most likely to have reduced the X-ray penetration depth into the NPs. Therefore, only signals from the outmost layers of the NPs were detected. In this regard, we believe

that oxidation of Ir was limited to the (near) surfaces of the NPs, while the NP cores remain metallic per the HRTEM findings. EDS elemental mapping of the NPs obtained after OER showed evenly distributed Rh and Ir signals, indicating segregation of Rh and Ir had not occurred during the electrocatalytic process (Figure S15). The contents of Ir for at least eight different NPs after the durability test were measured to be 70.0 ±1.7% by EDS, in close agreement with the composition of NPs before durability tests (75.7 ±3.6%). TEM images also show no measurable particle size or morphological changes; a small minority of NPs were found to have begun to agglomerate on the Vulcan support (Figure S16). Together, these observations suggest that Rh-Ir alloy NPs supported on VXC exhibited excellent stability under acidic OER conditions.

CONCLUSION

In summary, we report a rational synthetic strategy towards the preparation of sub-10 nm Rh-Ir nanoparticles as highly efficient OER catalysts under acidic conditions. The synthesis of Rh-Ir nanoparticles with homogeneously alloyed structures and tunable compositions was demonstrated. Benefiting from the advantages of microwave-assisted synthesis, $Rh_xIr_{(100-x)}$ NPs were rapidly and easily prepared over a broad compositional range; the NPs show excellent stability upon deposition on Vulcan carbon, to provide ideal model materials for electrochemical OER studies. Combined experimental and theoretical studies demonstrated that smaller binding energy gap of O and OOH intermediates was obtained through alloying 22% Rh into Ir, which resulted in a significant enhancement of OER performance, reflected by a 48 mV decrease in the overpotential to reach a 10 mA cm^{-2} current density and a mass activity that was three times higher than a comparable Ir NP catalyst. No obvious loss in OER activity was observed after 2000 cycles, indicating that the carbon-supported Rh-Ir alloy NPs are highly stable in an acidic electrolyte. The present work

provides the thorough study of an unexplored Rh-Ir alloy NP system and also offers fundamental understandings of composition-binding energy-electrocatalytic performance relationships.

METHODS

Synthesis of $Rh_xIr_{(100-x)}$ NPs and $Rh_xIr_{(100-x)}$/VXC catalysts. $Rh_xIr_{(100-x)}$ NPs with different compositions were prepared using a polyol method. In all reactions, PVP (0.45 mmol based on monomer) was pre-dissolved in 15.0 ml ethylene glycol and heated to 150 °C in a 50 ml round bottle flask equipped with a reflux condenser under constant magnetic stirring (450 rpm). The whole reaction system was inside a CEM-MARS-5 microwave reactor operating at 800 W. After the temperature was stabilized at 150 °C, a mixed metal precursor solution was delivered directly above of the stirred solution through a Teflon cannula (I.D.= 1.0 mm). The overall amount of metal precursors was 0.1 mmol for all the reactions and the addition rate of metal precursors was strictly controlled to be 6.0 $mmol_{Rh+Ir}$ h^{-1} by a syringe pump. The reaction mixture was heated for 30 min under continuous microwave irradiation, followed by quenching in an ice-water batch to stop any further growth of the nanoparticles. The PVP-capped nanoparticles were isolated by centrifugation with the addition of excess acetone. The NPs were twice re-dispersed in ethanol and precipitated with excess hexanes by centrifugation. The product was then dried under vacuum and stored as amorphous glass. $Rh_xIr_{(100-x)}$/VXC catalysts were prepared by adding $Rh_xIr_{(100-x)}$NPs dispersed in EG (40 ml) to VXC-72R carbon black dispersed in ethanol (250 ml), followed by stirring at room temperature for 24 h. The composite was collected on a nylon membrane (0.22 μm pore size) by vacuum filtration, washed copiously with ethanol and dried under vacuum.

Characterizations. Powder X-ray diffraction (PXRD) patterns of the NPs were collected on a Rigaku R-axis Spider diffractometer with a Cu Kα source (λ = 1.5406 Å) operating at 40 kV and 40 mA. Transmission electron microscope (TEM) images for NPs and catalysts were taken on a

FEI Tecnai transmission electron microscope operating at 80 kV. TEM samples were prepared by drop-casting ethanolic dispersions of NPs or catalysts on a 200 mesh Cu grids (200 mesh Cu/Formvar; Ted Pella, Inc.) and allowing the solvent to evaporate. HRTEM images, EDS elemental mapping and line scan profiles were collected on a JEOL 2010F transmission electron microscope operating at 200 kV. ICP-OES was conducted on an Agilent Varian 710-ES inductively coupled plasma optical emission spectroscopy. ICP-OES samples of the NPs were prepared by digesting NPs in 12 ml mixture of HCl (trace metal grade) and H_2O_2 (v:v=3:1) in Teflon-coated EasyPrep vessels at 200 °C for 3 h. The whole digestion was performed in a CEM-MARS-5 microwave reactor. The preparation of ICP-OES samples for $Rh_xIr_{(100-x)}$/VXC-72R catalysts was the same except that the digestion time was extended to 20 h for complete dissolution of carbon support. X-ray photoelectron spectra (XPS) were collected on a Kratos X-ray photoelectron spectrometer with Al Kα source (1486.6 eV). The XPS samples for NPs were prepared by drop-casting ethanolic dispersion of the NPs on indium-tin oxide (ITO) coated glass wafers and allowing complete evaporation of ethanol.

Electrochemical Measurements. Electrochemical measurements were conducted in a three-electrode electrochemical cell using saturated Ag/AgCl electrode as the reference electrode, a platinum wire as the counter electrode and the sample modified glassy carbon electrode (GCE) as the working electrode on a BioLogic Instrument (BioLogic VMP-3model). All the OER measurements performed on glassy carbon electrode (GCE) were under identical conditions with the same catalyst mass loading: 4 mg of catalyst and 40 μL of 5 wt% Nafion solution were dispersed in 0.96 mL ethanol solvent by 30 min sonication to form a homogeneous ink. 5 μL of the catalyst dispersion was then transferred onto the GCE *via* a drop casting method. The mass loading of catalyst on GCE is 0.28 mg cm^{-2}. Linear sweep voltammograms (LSV) polarization

curves were obtained by sweeping the potential from 1.20 V to 1.80 V (*vs*. RHE) at a sweep rate of 10 mV s^{-1} in 0.5 M H_2SO_4. The cathodic response was IR-corrected for ohmic loss throughout the system (Figure S17). For the chronoamperometric test of $Rh_{22}Ir_{78}$/VXC and commercial Ir/C, a static overpotential was fixed at 1.53 V (*vs*. RHE) for a certain time during the continuous electrocatalytic process to obtain the curve of the time dependence of the current density. The cyclic voltammetry (CV) curves for determining the electrochemical surface area of Rh-Ir electrocatalysts were obtained by sweeping the potential from 0.05 V to 1.00 V (*vs*. RHE) at a sweep rate of 50 mV s^{-1} in Ar-saturated 0.5 M H_2SO_4. The H desorption and adsorption regions from ~0.05 to ~0.3 V (*vs*. RHE) are integrated after subtracting the double-layer current density. The resulting coulombic charges are averaged and further divided by the specific charge to give the ECSA of catalysts.

Computational and Modeling Method. All the DFT calculations were performed using the Vienna *Ab initio* Simulation Package (VASP). Kohn-Sham wave functions were expanded in a plane wave basis to describe the valance electrons.[64] Core electrons were described within the projector augmented-wave (PAW) framework.[65] Electronic exchange and correlation were described by the generalized gradient approximation (GGA) with the Perdew-Burke-Ernzerhof (PBE) functional.[66] The Brillouin zone was sampled with a (3 × 3 × 1) Monkhorst-Pack *k*-point mesh.[67] The kinetic energy cutoff for the computations was set as 400 eV and the force convergence criteria was set as 0.05 eV/Å. Spin-polarization was tested and only included in the calculation of the oxygen molecule. Both the zero-point energy and entropic corrections (with the temperature of 298.15 K) were included in the free energy calculations. All the calculated surfaces were modeled as slabs with four-layer (4 × 4) unit cells. A vacuum layer of at least 12 Å was applied in the *z*-direction to separate images. For each slab model, the topmost two layers were

able to relax, while the bottom two layers were kept fixed in bulk positions. In sum, four types of surfaces [Rh(111), $Rh_{0.50}Ir_{0.50}$(111), $Rh_{0.25}Ir_{0.75}$(111), and Ir(111)] were studied in this paper; $Rh_{0.50}Ir_{0.50}$(111) and $Rh_{0.25}Ir_{0.75}$(111) were modeled as ordered alloys. The lattice constant of each surface was calculated using the Vegard's law according to the composition of the surface.[32,68] To evaluate the OER activity on a synthesized alloy surface, a bare (111) surface of strong-binding metal (*e.g.*, Ni, Ir, and Rh) is difficult to stabilize the adsorption of OOH. Therefore, OER activity could be ill-evaluated only on a bare model surface. Wang *et al.* showed that an oxygen-covered surface is a suitable model that simulates the slightly oxidized metallic surface under OER reaction conditions, having qualitative agreement with the experimentally measured onset potentials on Ni-Fe bimetallic alloy surfaces.[69] Therefore, in our study, all DFT calculations were conducted with an oxygen-covered surface with the oxygen coverage of 75%, which matches XPS results that the surface of Rh-Ir NP is slightly oxidized (Figure 1B). The theoretical overpotential η was calculated using the following equation:

$$\eta = \mathrm{Max}\{\Delta G_1, \Delta G_2, \Delta G_3, \Delta G_4\}/e - 1.23V$$

where ΔG_1- ΔG_4 represent the reaction free energies of four elementary steps for OER.[60] The O and OH binding energies E_b were calculated using the following equation:

$$E_b = E_{ads*} - E_* - E_{ads}$$

where E_{ads*} is the energy of surface with the target adsorbate, E_* is the energy of the surface without the target adsorbate, and E_{ads} is the energy of the adsorbate in vacuum (calculated with spin-polarization).

ASSOCIATED CONTENT

Supporting information

Detailed experimental and computational methods, further, TEM images, EDS mapping and spectrum, XPS spectrum, electrochemical calculations, and calculation results. This material is available free of charge *via* the Internet at http://pubs.acs.org.

AUTHOR INFORMATION

Corresponding Author

*Email: henkelman@utexas.edu (G. Henkelman).

*Email: smh@cm.utexas.edu (S. M. Humphrey).

*Email: ghyu@austin.utexas.edu (G. Yu).

ORCID

Zhiwei Fang: 0000-0001-8826-8834

Graeme Henkelman: 0000-0002-0336-7153

Simon M. Humphrey: 0000-0001-5379-4623

Guihua Yu: 0000-0002-3253-0749

Author Contributions

§H. G. and Z. F. contributed equally to this project.

ACKNOWLEDGMENT

The authors thank Dr. Hugo Celio (XPS) and Dr. Karalee Jarvis (EDS) for analytical assistance. G.H. acknowledges the funding support from the National Science Foundation (CHE-1807847) and the Welch Foundation (F-1841). S.M.H. acknowledges the funding support from the National Science Foundation (CHE-1807847) and the Welch Foundation (F-1731). G.Y. acknowledges the

funding support from the US Department of Energy, Office of Science, Basic Energy Sciences, under Award DE-SC0019019, Alfred P. Sloan Foundation and Camille Dreyfus Teacher-Scholar Award. Computational resources were provided by the Texas Advanced Computing Center.

REFERENCES

(1) Tahir, M.; Pan, L.; Idrees, F.; Zhang, X.; Wang, L.; Zou, J. J.; Wang, Z. L. Electrocatalytic Oxygen Evolution Reaction for Energy Conversion and Storage: A Comprehensive Review. *Nano Energy* **2017**, *37*, 136–157.

(2) Huang, Z. F.; Wang, J.; Peng, Y.; Jung, C. Y.; Fisher, A.; Wang, X. Design of Efficient Bifunctional Oxygen Reduction/Evolution Electrocatalyst: Recent Advances and Perspectives. *Adv. Energy Mater.* **2017**, *7*, 1700544.

(3) Zhu, Y.; Peng, L.; Fang, Z.; Yan, C.; Zhang, X.; Yu, G. Structural Engineering of 2D Nanomaterials for Energy Storage and Catalysis. *Adv. Mater.* **2018**, *30*, 1706347.

(4) Suen, N. T.; Hung, S. F.; Quan, Q.; Zhang, N.; Xu, Y. J.; Chen, H. M. Electrocatalysis for the Oxygen Evolution Reaction: Recent Development and Future Perspectives. *Chem. Soc. Rev.* **2017**, *46*, 337–365.

(5) Jiao, Y.; Zheng, Y.; Jaroniec, M.; Qiao, S. Z. Design of Electrocatalysts for Oxygen- and Hydrogen-Involving Energy Conversion Reactions. *Chem. Soc. Rev.* **2015**, *44*, 2060–2086.

(6) Dionigi, F.; Strasser, P. NiFe-Based (Oxy)Hydroxide Catalysts for Oxygen Evolution Reaction in Non-Acidic Electrolytes. *Adv. Energy Mater.* **2016**, *6*, 1600621.

(7) Friebel, D.; Louie, M. W.; Bajdich, M.; Sanwald, K. E.; Cai, Y.; Wise, A. M.; Cheng, M. J.; Sokaras, D.; Weng, T. C.; Alonso-Mori, R.; Davis, R. C.; Bargar, J. R.; Nørskov, J. K.;

Nilsson, A.; Bell, A. T. Identification of Highly Active Fe Sites in (Ni,Fe)OOH for Electrocatalytic Water Splitting. *J. Am. Chem. Soc.* **2015**, *137*, 1305–1313.

(8) Fang, Z.; Peng, L.; Lv, H.; Zhu, Y.; Yan, C.; Wang, S.; Kalyani, P.; Wu, X.; Yu, G. Metallic Transition Metal Selenide Holey Nanosheets for Efficient Oxygen Evolution Electrocatalysis. *ACS Nano* **2017**, *11*, 9550–9557.

(9) Li, P.; Jin, Z.; Qian, Y.; Fang, Z.; Xiao, D.; Yu, G. Probing Enhanced Site Activity of Co-Fe Bimetallic Sub-Nanoclusters Derived from Dual Cross-Linked Hydrogels for Oxygen Electrocatalysis. *ACS Energy Lett.* **2019**, *4*, 1793–1802.

(10) Xu, K.; Chen, P.; Li, X.; Tong, Y.; Ding, H.; Wu, X.; Chu, W.; Peng, Z.; Wu, C.; Xie, Y. Metallic Nickel Nitride Nanosheets Realizing Enhanced Electrochemical Water Oxidation. *J. Am. Chem. Soc.* **2015**, *137*, 4119–4125.

(11) Fang, Z.; Zhang, A.; Wu, P.; Yu, G. Inorganic Cyanogels and Their Derivatives for Electrochemical Energy Storage and Conversion. *ACS Mater. Lett.* **2019**, *1*, 158–170.

(12) Fang, Z.; Peng, L.; Qian, Y.; Zhang, X.; Xie, Y.; Cha, C.; Yu, G. Dual Tuning of Ni–Co–A (A = P, Se, O) Nanosheets by Anion Substitution and Holey Engineering for Efficient Hydrogen Evolution. *J. Am. Chem. Soc.* **2018**, *140*, 5241–5247.

(13) Jiang, N.; You, B.; Sheng, M.; Sun, Y. Electrodeposited Cobalt-Phosphorous-Derived Films as Competent Bifunctional Catalysts for Overall Water Splitting. *Angew. Chem., Int. Ed.* **2015**, *54*, 6251–6254.

(14) Wang, X.; Vasileff, A.; Jiao, Y.; Zheng, Y.; Qiao, S. Z. Electronic and Structural Engineering of Carbon-Based Metal-Free Electrocatalysts for Water Splitting. *Adv. Mater.*

2019, *31*, 1803625.

(15) Spöri, C.; Kwan, J. T. H.; Bonakdarpour, A.; Wilkinson, D. P.; Strasser, P. The Stability Challenges of Oxygen Evolving Catalysts: Towards a Common Fundamental Understanding and Mitigation of Catalyst Degradation. *Angew. Chem., Int. Ed.* **2017**, *56*, 5994–6021.

(16) Reier, T.; Nong, H. N.; Teschner, D.; Schlögl, R.; Strasser, P. Electrocatalytic Oxygen Evolution Reaction in Acidic Environments-Reaction Mechanisms and Catalysts. *Adv. Energy Mater.* **2017**, *7*, 1601275.

(17) Sardar, K.; Petrucco, E.; Hiley, C. I.; Sharman, J. D. B.; Wells, P. P.; Russell, A. E.; Kashtiban, R. J.; Sloan, J.; Walton, R. I. Water-Splitting Electrocatalysis in Acid Conditions Using Ruthenate-Iridate Pyrochlores. *Angew. Chem., Int. Ed.* **2014**, *53*, 10960–10964.

(18) McCrory, C. C. L.; Jung, S.; Ferrer, I. M.; Chatman, S. M.; Peters, J. C.; Jaramillo, T. F. Benchmarking Hydrogen Evolving Reaction and Oxygen Evolving Reaction Electrocatalysts for Solar Water Splitting Devices. *J. Am. Chem. Soc.* **2015**, *137*, 4347–4357.

(19) Wei, C.; Rao, R. R.; Peng, J.; Huang, B.; Stephens, I. E. L.; Risch, M.; Xu, Z. J.; Shao-Horn, Y. Recommended Practices and Benchmark Activity for Hydrogen and Oxygen Electrocatalysis in Water Splitting and Fuel Cells. *Adv. Mater.* **2019**, *31*, 1806296.

(20) Antolini, E. Iridium as Catalyst and Cocatalyst for Oxygen Evolution/Reduction in Acidic Polymer Electrolyte Membrane Electrolyzers and Fuel Cells. *ACS Catal.* **2014**, *4*, 1426–1440.

(21) Shan, J.; Guo, C.; Zhu, Y.; Chen, S.; Song, L.; Jaroniec, M.; Zheng, Y.; Qiao, S. Z. Charge-Redistribution-Enhanced Nanocrystalline Ru@IrO_x Electrocatalysts for Oxygen Evolution in Acidic Media. *Chem* **2019**, *5*, 445–459.

(22) She, Z. W.; Kibsgaard, J.; Dickens, C. F.; Chorkendorff, I.; Nørskov, J. K.; Jaramillo, T. F. Combining Theory and Experiment in Electrocatalysis: Insights into Materials Design. *Science.* **2017**, *355*, 4998.

(23) Pfeifer, V.; Jones, T. E.; Velasco Vélez, J. J.; Arrigo, R.; Piccinin, S.; Hävecker, M.; Knop-Gericke, A.; Schlögl, R. *In Situ* Observation of Reactive Oxygen Species Forming on Oxygen-Evolving Iridium Surfaces. *Chem. Sci.* **2017**, *8*, 2143–2149.

(24) Grimaud, A.; May, K. J.; Carlton, C. E.; Lee, Y. L.; Risch, M.; Hong, W. T.; Zhou, J.; Shao-Horn, Y. Double Perovskites as a Family of Highly Active Catalysts for Oxygen Evolution in Alkaline Solution. *Nat. Commun.* **2013**, *4*, 2439.

(25) Calle-Vallejo, F.; Inoglu, N. G.; Su, H. Y.; Martínez, J. I.; Man, I. C.; Koper, M. T. M.; Kitchin, J. R.; Rossmeisl, J. Number of Outer Electrons as Descriptor for Adsorption Processes on Transition Metals and Their Oxides. *Chem. Sci.* **2013**, *4*, 1245–1249.

(26) Diaz-Morales, O.; Raaijman, S.; Kortlever, R.; Kooyman, P. J.; Wezendonk, T.; Gascon, J.; Fu, W. T.; Koper, M. T. M. Iridium-Based Double Perovskites for Efficient Water Oxidation in Acid Media. *Nat. Commun.* **2016**, *7*, 12363.

(27) Reier, T.; Pawolek, Z.; Cherevko, S.; Bruns, M.; Jones, T.; Teschner, D.; Selve, S.; Bergmann, A.; Nong, H. N.; Schlögl, R.; Mayrhofer, K. J. J.; Strasser, P. Molecular Insight in Structure and Activity of Highly Efficient, Low-Ir Ir-Ni Oxide Catalysts for

Electrochemical Water Splitting (OER). *J. Am. Chem. Soc.* **2015**, *137*, 13031–13040.

(28) Feng, J.; Lv, F.; Zhang, W.; Li, P.; Wang, K.; Yang, C.; Wang, B.; Yang, Y.; Zhou, J.; Lin, F.; Wang, G.-C.; Guo, S. Iridium-Based Multimetallic Porous Hollow Nanocrystals for Efficient Overall-Water-Splitting Catalysis. *Adv. Mater.* **2017**, *29*, 1703798.

(29) Shan, J.; Ling, T.; Davey, K.; Zheng, Y. Qiao, S. Z. Transition-Metal-Doped RuIr Bifunctional Nanocrystals for Overall Water Splitting in Acidic Environments. *Adv. Mater.* **2017**, *31*, 1900510.

(30) Li, H.; Henkelman, G. Dehydrogenation Selectivity of Ethanol on Close-Packed Transition Metal Surfaces: A Computational Study of Monometallic, Pd/Au, and Rh/Au Catalysts. *J. Phys. Chem. C* **2017**, *121*, 27504–27510.

(31) Li, H.; Luo, L.; Kunal, P.; Bonifacio, C. S.; Duan, Z.; Yang, J. C.; Humphrey, S. M.; Crooks, R. M.; Henkelman, G. Oxygen Reduction Reaction on Classically Immiscible Bimetallics: A Case Study of RhAu. *J. Phys. Chem. C* **2018**, *122*, 2712–2716.

(32) Li, H.; Evans, E. J.; Mullins, C. B.; Henkelman, G. Ethanol Decomposition on Pd-Au Alloy Catalysts. *J. Phys. Chem. C* **2018**, *122*, 22024–22032.

(33) Li, H.; Shin, K.; Henkelman, G. Effects of Ensembles, Ligand, and Strain on Adsorbate Binding to Alloy Surfaces. *J. Chem. Phys.* **2018**, *149*, 174705.

(34) Yi, C.-W.; Chen, M.; Goodman, D. W.; Kumar, D. The Promotional Effect of Gold in Catalysis by Palladium-Gold. *Science* **2005**, *310*, 291–293.

(35) Mavrikakis, M.; Hammer, B.; Nørskov, J. K. Effect of Strain on the Reactivity of Metal Surfaces. *Phys. Rev. Lett.* **1998**, *81*, 2819–2822.

(36) Luo, M.; Guo, S. Strain-Controlled Electrocatalysis on Multimetallic Nanomaterials. *Nat. Rev. Mater.* **2017**, *2*, 17059.

(37) Lv, F.; Feng, J.; Wang, K.; Dou, Z.; Zhang, W.; Zhou, J.; Yang, C.; Luo, M.; Yang, Y.; Li, Y.; Gao, P.; Guo, S. Iridium-Tungsten Alloy Nanodendrites as pH-Universal Water-Splitting Electrocatalysts. *ACS Cent. Sci.* **2018**, *4*, 1244–1252.

(38) Pi, Y.; Shao, Q.; Wang, P.; Guo, J.; Huang, X. General Formation of Monodisperse IrM (M=Ni, Co, Fe) Bimetallic Nanoclusters as Bifunctional Electrocatalysts for Acidic Overall Water Splitting. *Adv. Funct. Mater.* **2017**, *27*, 1700886.

(39) Wang, F.; Kusada, K.; Wu, D.; Yamamoto, T.; Toriyama, T.; Matsumura, S.; Nanba, Y.; Koyama, M.; Kitagawa, H. Solid-Solution Alloy Nanoparticles of the Immiscible Iridium-Copper System with a Wide Composition Range for Enhanced Electrocatalytic Applications. *Angew. Chem., Int. Ed.* **2018**, *57*, 4505–4509.

(40) Franke, P., Neuschütz, D. *Thermodynamic Properties of Inorganic Materials·Binary Systems. Part 5: Binary Systems Supplement 1*. Springer: Berlin Heidelberg, **2007**.

(41) Guo, H.; Li, H.; Jarvis, K.; Wan, H.; Kunal, P.; Dunning, S. G.; Liu, Y.; Henkelman, G.; Humphrey, S. M. Microwave-Assisted Synthesis of Classically Immiscible Ag-Ir Alloy Nanoparticle Catalysts. *ACS Catal.* **2018**, *8*, 11386–11397.

(42) Miles, M. H.; Thomason, M. A. Periodic Variations of Overvoltages for Water Electrolysis in Acid Solutions from Cyclic Voltammetric Studies. *J. Electrochem. Soc.* **1976**, *123*, 1459–1461.

(43) Cherevko, S.; Zeradjanin, A. R.; Topalov, A. A.; Kulyk, N.; Katsounaros, I.; Mayrhofer, K.

J. J. Dissolution of Noble Metals during Oxygen Evolution in Acidic Media. *ChemCatChem* **2014**, *6*, 2219–2223.

(44) Freakley, S. J.; Ruiz-Esquius, J.; Morgan, D. J. The X-Ray Photoelectron Spectra of Ir, IrO_2 and $IrCl_3$ Revisited. *Surf. Interface Anal.* **2017**, *49*, 794–799.

(45) Tao, A. R.; Habas, S.; Yang, P. Shape Control of Colloidal Metal Nanocrystals. *Small* **2008**, *4*, 310–325.

(46) Luo, M.; Hong, Y.; Yao, W.; Huang, C.; Xu, Q.; Wu, Q. Facile Removal of Polyvinylpyrrolidone (PVP) Adsorbates from Pt Alloy Nanoparticles. *J. Mater. Chem. A* **2015**, *3*, 2770–2775.

(47) Lee, Y.; Suntivich, J.; May, K. J.; Perry, E. E.; Shao-Horn, Y. Synthesis and Activities of Rutile IrO_2 and RuO_2 Nanoparticles for Oxygen Evolution in Acid and Alkaline Solutions. *J. Phys. Chem. Lett.* **2012**, *3*, 399–404.

(48) Lim, J.; Park, D.; Jeon, S. S.; Roh, C. W.; Choi, J.; Yoon, D.; Park, M.; Jung, H.; Lee, H. Ultrathin IrO_2 Nanoneedles for Electrochemical Water Oxidation. *Adv. Funct. Mater.* **2018**, *28*, 1704796.

(49) Yang, L.; Yu, G.; Ai, X.; Yan, W.; Duan, H.; Chen, W.; Li, X.; Wang, T.; Zhang, C.; Huang, X.; Chen, J.-S.; Zou, X. Efficient Oxygen Evolution Electrocatalysis in Acid by a Perovskite with Face-Sharing IrO_6 Octahedral Dimers. *Nat. Commun.* **2018**, *9*, 5236.

(50) Oh, H. S.; Nong, H. N.; Reier, T.; Bergmann, A.; Gliech, M.; Ferreira De Araújo, J.; Willinger, E.; Schlögl, R.; Teschner, D.; Strasser, P. Electrochemical Catalyst-Support Effects and Their Stabilizing Role for IrO_x Nanoparticle Catalysts during the Oxygen

Evolution Reaction. *J. Am. Chem. Soc.* **2016**, *138*, 12552–12563.

(51) Wang, C.; Sui, Y.; Xiao, G.; Yang, X.; Wei, Y.; Zou, G.; Zou, B. Synthesis of Cu-Ir Nanocages with Enhanced Electrocatalytic Activity for the Oxygen Evolution Reaction. *J. Mater. Chem. A* **2015**, *3*, 19669–19673.

(52) Wang, C.; Sui, Y.; Xu, M.; Liu, C.; Xiao, G.; Zou, B. Synthesis of Ni-Ir Nanocages with Improved Electrocatalytic Performance for the Oxygen Evolution Reaction. *ACS Sustain. Chem. Eng.* **2017**, *5*, 9787–9792.

(53) Godínez-Salomón, F.; Albiter, L.; Alia, S. M.; Pivovar, B. S.; Camacho-Forero, L. E.; Balbuena, P. B.; Mendoza-Cruz, R.; Arellano-Jimenez, M. J.; Rhodes, C. P. Self-Supported Hydrous Iridium-Nickel Oxide Two-Dimensional Nanoframes for High Activity Oxygen Evolution Electrocatalysts. *ACS Catal.* **2018**, *8*, 10498–10520.

(54) Pi, Y.; Guo, J.; Shao, Q.; Huang, X. Highly Efficient Acidic Oxygen Evolution Electrocatalysis Enabled by Porous Ir-Cu Nanocrystals with Three-Dimensional Electrocatalytic Surfaces. *Chem. Mater.* **2018**, *30*, 8571–8578.

(55) Nong, H. N.; Oh, H. S.; Reier, T.; Willinger, E.; Willinger, M. G.; Petkov, V.; Teschner, D.; Strasser, P. Oxide-Supported $IrNiO_x$ Core-Shell Particles as Efficient, Cost-Effective, and Stable Catalysts for Electrochemical Water Splitting. *Angew. Chem., Int. Ed.* **2015**, *54*, 2975–2979.

(56) Park, J.; Sa, Y. J.; Baik, H.; Kwon, T.; Joo, S. H.; Lee, K. Iridium-Based Multimetallic Nanoframe@Nanoframe Structure: An Efficient and Robust Electrocatalyst toward Oxygen Evolution Reaction. *ACS Nano* **2017**, *11*, 5500–5509.

(57) Jin, H.; Hong, Y.; Yoon, J.; Oh, A.; Chaudhari, N. K.; Baik, H.; Joo, S. H.; Lee, K. Lanthanide Metal-Assisted Synthesis of Rhombic Dodecahedral MNi (M=Ir and Pt) Nanoframes toward Efficient Oxygen Evolution Catalysis. *Nano Energy* **2017**, *42*, 17–25.

(58) Nong, H. N.; Gan, L.; Willinger, E.; Teschner, D.; Strasser, P. IrO_x Core-Shell Nanocatalysts for Cost- and Energy-Efficient Electrochemical Water Splitting. *Chem. Sci.* **2014**, *5*, 2955–2963.

(59) Kwon, T.; Hwang, H.; Sa, Y. J.; Park, J.; Baik, H.; Joo, S. H.; Lee, K. Cobalt Assisted Synthesis of IrCu Hollow Octahedral Nanocages as Highly Active Electrocatalysts toward Oxygen Evolution Reaction. *Adv. Funct. Mater.* **2017**, *27*, 1604688.

(60) Man, I. C.; Su, H. Y.; Calle-Vallejo, F.; Hansen, H. A.; Martínez, J. I.; Inoglu, N. G.; Kitchin, J.; Jaramillo, T. F.; Nørskov, J. K.; Rossmeisl, J. Universality in Oxygen Evolution Electrocatalysis on Oxide Surfaces. *ChemCatChem* **2011**, *3*, 1159–1165.

(61) Tritsaris, G. A.; Greeley, J.; Rossmeisl, J.; Nørskov, J. K. Atomic-Scale Modeling of Particle Size Effects for the Oxygen Reduction Reaction on Pt. *Catal. Letters* **2011**, *141*, 909–913.

(62) Wannakao, S.; Maihom, T.; Kongpatpanich, K.; Limtrakul, J.; Promarak, V. Halogen Substitutions Leading to Enhanced Oxygen Evolution and Oxygen Reduction Reactions in Metalloporphyrin Frameworks. *Phys. Chem. Chem. Phys.* **2017**, *19*, 29540–29548.

(63) Li, H.; Guo, S.; Shin, K.; Wong, M. S.; Henkelman, G. Design of a Pd−Au Nitrite Reduction Catalyst by Identifying and Optimizing Active Ensembles. *ACS Catal.* **2019**, *9*, 7957–7966.

(64) Pople, J. A.; Gill, P. M. W.; Johnson, B. G. Kohn-Sham Density-Functional Theory within

a Finite Basis Set. *Chem. Phys. Lett.* **1992**, *199*, 557–560.

(65) Blöchl, P. E. Projector Augmented-Wave Method. *Phys. Rev. B* **1994**, *50*, 17953–17979.

(66) Perdew, J. P.; Burke, K.; Ernzerhof, M. Generalized Gradient Approximation Made Simple. *Phys. Rev. Lett.* **1996**, *77*, 3865–3868.

(67) Monkhorst, H. J.; Pack, J. D. Special Points Fro Brillouin-Zone Integretions. *Phys. Rev. B* **1976**, *13*, 5188–5192.

(68) Ashcroft, N. W.; Denton, A. R. Vegard's Law. *Phys. Rev. A* **1991**, *43*, 3161–3164.

(69) Wang, A.; Zhao, Z.; Hu, D.; Niu, J.; Zhang, M.; Yan, K.; Lu, G. Tuning the Oxygen Evolution Reaction on a Nickel-Iron Alloy: *via* Active Straining. *Nanoscale* **2019**, *11*, 426–430.

GRAPHIC TABLE OF CONTENTS